





Original Paper

Kinetics of Mg-Ni saponite crystallization from precursor mixtures

Chaoqun Zhang^{1,2}, Alain Decarreau², Philippe Blanc³, Fabien Baron², Yuhuan Yuan¹, Qi Tao¹ , Brian Gregoire² ,
Jianxi Zhu¹ , Hongping He¹ and Sabine Petit² 

¹CAS Key Laboratory of Mineralogy and Metallogeny/Guangdong Provincial Key Laboratory of Mineral Physics and Materials, Guangzhou Institute of Geochemistry, Chinese Academy of Sciences, 510640 Guangzhou, China; ²CNRS, Université de Poitiers, Institut de Chimie des Milieux et Matériaux de Poitiers-IC2MP, 86022 Poitiers, France and ³Bureau de recherches géologiques et minières (BRGM), 3 Avenue C. Guillemin, BP6009, F-45060 Orléans, France

Abstract

Smectite growth is of importance across various fields due to its abundance on the surface of both Earth and Mars. However, the impact of the crystallinity of initial materials on smectite growth processes remains poorly understood. In this study, the kinetic processes of smectite growth were examined via experimental synthesis of trioctahedral Mg-Ni saponites. Mg-Ni saponites were synthesized using mixed precursors, specifically end-member Mg-saponite and Ni-saponite, which exhibit different crystallinities. The crystal chemistry and morphology of samples were analyzed using X-ray diffraction, Fourier-transform infrared spectroscopy, and high-angle annular dark-field scanning transmission electron microscopy. The experimental results converge towards these main conclusions: (i) the formation of Mg-Ni saponite solid solutions are promoted when the precursors are small particles, whereas large-particle precursors limit their own dissolution and do not yield Mg-Ni saponite solid solutions under the experimental conditions; (ii) because Ni exhibits a greater stability within the saponite structure compared to Mg, the Mg-Ni-saponite solid solutions formed more easily from the mixture of Ni-saponite germs and well-crystallized Mg-saponite precursors than from the mixture of Mg-saponite germs and well-crystallized Ni-saponite precursors; (iii) the dissolution extent (DE) of precursor mixtures increases with longer synthesis time, higher synthesis temperature, and larger gap between synthesis temperature of precursors and of samples, and stabilizes once it reaches a certain value. Thus DE can be used to estimate the kinetics of Mg-Ni saponite crystallization from precursor mixtures. These results obtained from the experimental Mg-Ni saponite system are useful for predicting the evolution processes of smectite in natural systems.

Keywords: clay minerals; crystal growth; Ni; Ni-Mg distribution coefficient; saponite; smectite; solid solution; synthesis

(Received: 18 April 2024; revised: 17 June 2024; accepted: 25 June 2024)

Introduction

Smectites have been studied across various topics such as material synthesis, environmental impact, and Martian surface evolution (Schoonheydt, 2002; Ehlmann et al., 2014; Ferrage, 2016; Besselink et al., 2020; Blukis et al., 2022). These clay minerals exhibit a wide range of compositions; different cations can occupy the tetrahedral sites (e.g. Si⁴⁺, Al³⁺, and Fe³⁺), octahedral sites (e.g. Al³⁺, Fe³⁺, Fe²⁺, Mg²⁺, Ni²⁺, Zn²⁺, and Li⁺), and interlayer space (e.g. Na⁺, K⁺, Ca²⁺, and Mg²⁺) (e.g. Warren et al., 1992; Hover et al., 1999; Yamada et al., 1999; Brigatti and Galán, 2013). Thus different smectites occur extensively in natural systems and are indicative of the environments where they formed. For example, Mg-Ni smectite appears in the lateritic profile as an abundant ore mineral (Gaudin et al., 2004; Butt and Cluzel, 2013; Fritsch et al., 2016; Mano et al., 2019). The Fe-Mg smectite on the surface of Mars contains

substantial information regarding paleoclimate changes (Carter et al., 2013; Ehlmann et al., 2013; Ehlmann et al., 2014; Michalski et al., 2015). Although smectite has attracted significant attention, its formation and growth processes are not well understood, and this limits our ability to infer the environment of clay formation.

Smectite synthesis in the laboratory with a controlled crystal chemistry enables the observation of the initial stages of smectite formation, which is scarcely observed in nature (Kloprogge et al., 1999; Zhang et al., 2010; Petit et al. 2017). Saponite is an easily synthesized trioctahedral smectite, and thus it is an ideal substance to explore the initial growth of smectite. Previous studies have reported that poorly ordered saponite can be obtained at low temperature and hours. Decarreau (1980, 1985) and Couty et al. (1981) demonstrated that the solid, formed at room temperature through the direct precipitation of Si and Mg salts, consisted of smectite germs (embryos of saponite crystals), associated within pseudo particles. Blukis et al. (2022) observed an instantaneous saponite nucleation at room temperature during the synthesis of Mg-saponite. They concluded that the saponite precursor, obtained through direct precipitation of Si, Al, and Mg salts, is very likely equivalent to the ‘clay nuclei’ as described by Decarreau (1980) in the stevensite and hectorite systems. Additionally, Besselink et al. (2020)

Corresponding authors: Hongping He and Sabine Petit; Emails: hehp@gig.ac.cn, sabine.petit@univ-poitiers.fr

Cite this article: Zhang C., Decarreau A., Blanc P., Baron F., Yuan Y., Tao Q., Gregoire B., Zhu J., He H., & Petit S. (2024). Kinetics of Mg-Ni saponite crystallization from precursor mixtures. *Clays and Clay Minerals* 72, e16, 1–10. <https://doi.org/10.1017/cmn.2024.29>

synthesized Mg-saponite at 95°C by reacting an amorphous (Si-Al) gel with MgCl₂, and saponite crystals emerged within a few hours. Literature shows that Mg-Ni saponite solid solutions were obtained in the range 25–500°C in a few weeks, indicating that they are much more stable than the mechanical mixture of end-members Ni-saponite and Mg-saponite (Decarreau, 1985; Zhang et al., 2021).

In this work, the Mg-Ni saponite (trioctahedral smectite) system was chosen because Mg and Ni saponites are easily synthesized (e.g. Zhang et al., 2020; Zhang et al., 2021; Zhang et al., 2022). Indeed, Ni²⁺ and Mg²⁺ have close ionic radii (0.69 and 0.72 Å, respectively), but different atomic mass of Mg (24.3 u) and Ni (58.7 u), which are valuable when performing crystal-chemistry analyses such as high-angle annular dark-field scanning transmission electron microscopy (HAADF-STEM) (Zhang et al., 2020; Zhang et al., 2021) and Fourier-transform infrared (FTIR) spectroscopy. Recording the stretching vibration of the structural OH using FTIR allows for systematic investigation of the octahedral cation distribution, because each structural OH group is linked to three neighboring *M* atoms (*M* being Mg and Ni in this case) (e.g. Petit et al., 2004; Petit and Madejová, 2013).

The Mg-Ni saponite system has been used to investigate the crystal growth of smectites (Zhang et al., 2020; Zhang et al., 2021; Zhang et al., 2022). Zhang et al. (2020) synthesized Mg-Ni saponites by hydrothermal treatment of Mg- and Ni-saponite precursors synthesized at 150°C, conducted at 220°C under autogenous pressure for durations ranging from 0.25 to 30 days. Those authors found that the cation distribution within Mg-Ni saponites tends to be random as the particle size increases and reaches a steady state after 15 days. Subsequently, Zhang et al. (2021) explored the formation conditions of Mg-Ni saponite from the mixture of various end-member saponites when the synthesis temperature increases. The results indicated that the formation of Mg-Ni smectite solid solutions is related to the temperature gap between the precursors and the synthesis, and the nature of the precursors. Based on previous studies, Zhang et al. (2022) examined the growth mechanisms of Mg-Ni saponite particles. The particle-size distribution suggests that Mg-Ni saponite grows mainly by dissolution-recrystallization, accompanied by particle attachment. Nevertheless, many questions remain, such as how the crystallinity of precursors affects the growth of Mg-Ni saponite. In this study, we examined the growth kinetics of Mg-Ni saponite from different precursors that have different crystallinities, and further discuss the factors that control the formation of Mg-Ni saponite.

Materials and methods

Synthesis of Mg- and Ni-saponite precursors

Mg- and Ni-saponite precursors were prepared through hydrothermal treatment of a co-precipitated gel with a theoretical Si:Al:Mg (or Ni) molar ratio of 3.7:0.3:3 according to the procedure described by Zhang et al. (2021), with hydrothermal treatment at RT (room temperature, 25°C), 150°C, and 220°C, respectively, for 24 h. The precursors, named as pMg_x and pNi_x (where *x* is temperature in °C), were obtained after filtration of the hydrothermal products and dried at 45°C. The Al occupancy of synthetic saponites has been studied in a previous study (He et al., 2014); the results indicate that Al prefers to occupy tetrahedral sites rather than octahedral sites, and there is only a little Al in the octahedral sheets, irrespective of the original amount of Al. For the present system, the amount of Al(VI) is estimated to be near 0.03, which is negligible. Note that the precursors synthesized at

25°C are composed of saponite germs exhibiting a short-range ordered structure, which predominantly appears with amorphous-like nature under X-ray diffraction (XRD) analysis (Couty et al., 1981; Besselinck et al., 2020). In this work, all precursors are assumed to consist solely of Mg- or Ni-saponite nanocrystals. Due to the small size of the saponite, Si-OH occurs on the edge of layers (Couty et al., 1981). Their structural formula can then be expressed as Na_{0.3}[Si_{3.7}Al_{0.3}][M²⁺₃]O_{10-ε}(OH)_{2+2ε}, where *M* represents Mg or Ni, and *ε* denotes the quantity of edge hydroxyl groups (OH). The value of *ε* decreases as the crystal size increases.

Synthesis of Mg-Ni saponites

The starting material was prepared by mixing an identical molar quantity of Mg- and Ni-saponite precursors (i.e. 0.11 g of pMg_x and 0.14 g pNi_x) in different combinations (pMg150 and pNi150, pMg220 and pNi220, pMg220 and pNi25, and pNi220 and pMg25).

The mixture of precursors was added to 30 mL of deionized water and stirred continuously at room temperature for 1 day. Suspensions of precursors were transferred to a polytetrafluoroethylene-lined autoclave and heated at 150 or 220°C for a period of 14–90 days. Four series of samples were obtained, i.e. Series (pMg150+pNi150)150, Series (pMg220+pNi220)220, Series (pMg220+pNi25)220, and Series (pNi220+pMg25)220. The obtained samples were washed by filtration and named (pMg_x+pNi_y)*T-t*, where *x* and *y* are the temperature of precursor formation; and *T* and *t* are the synthesis temperature and the synthesis time of samples, respectively (see sample name in Tables 1–3). For example, (pMg150+pNi150)150-*t* refers to the Mg-saponite precursor, initially synthesized hydrothermally at 150°C, combined in a 1:1 molar ratio with the Ni-saponite precursor synthesized at 150°C, and subsequently aged hydrothermally at 150°C for *t* days. Samples with *t*=0 days, were obtained by filtration of the mixtures of precursors after 1 day of stirring at room temperature. All samples were dried at 45°C. The expected structural formula of the bulk end of synthesis saponite is Na_{0.3}[Si_{3.7}Al_{0.3}][Ni_{1.5}Mg_{1.5}]O₁₀(OH)₂.

Methods

Powder XRD patterns were obtained on a Bruker D8 advance diffractometer (CuKα radiation, 40 kV and 40 mA) over the range of 2–65°2θ with a 0.025°2θ step size and 0.6 s per step. The mean size of coherent diffracting domains in the plane of layers, i.e. Crystal Size Dimension (CSD), was measured from the (06,33) reflection using the Scherrer equation (Table 1).

Inductively coupled plasma-optical emission spectroscopy (Thermo Fisher Scientific iCAP 7400 series ICP-OES) was used to determine the elemental composition of the experimental solutions after the hydrothermal treatment. Ten milliliters of solution was diluted in 2 wt.% HNO₃ to measure aqueous concentrations (Si, Mg, Ni, and Al) in the linear range of the calibration curves. The partition coefficient $D_{(Ni-Mg)} = (Ni/Mg)_{solid} / (Ni/Mg)_{liquid}$ was estimated based on the solution chemistry after synthesis (Decarreau, 1985) (see results in Table 2).

Mid-infrared (MIR) spectra were obtained using a Nicolet 6700 FT-IR spectrometer equipped with an Ever-Glo source, a KBr beam splitter, and a DTGS-KBr detector. MIR spectra resulted from the average of 100 scans acquired in transmission mode over the 400–4000 cm⁻¹ range with a resolution of 4 cm⁻¹. KBr pellets were prepared with 1 mg of sample and 150 mg of

Table 1. Crystal size dimension (CSD, Å) in the *ab* plane of saponite samples from the (06,33) reflection using the Scherrer equation

Series	Samples	CSD	CSD pMgx	CSD pNix	CSD mean*
(pMg150+pNi150)150	(pMg150+pNi150)150–0d	57	54	62	58
	(pMg150+pNi150)150–14d	82			
	(pMg150+pNi150)150–30d	101			
(pMg220+pNi220)220	(pMg220+pNi220)220–0d	121	119	125	122
	(pMg220+pNi220)220–30d	121			
	(pMg220+pNi220)220–90d	129			
(pNi220+pMg25)220	(pNi220+pMg25)220–0d	113	24	125	75
	(pNi220+pMg25)220–60d	151			
(pMg220+pNi25)220	(pNi25+pMg220)220–0d	101	119	31	75
	(pNi25+Mg220)220–60d	151			

*CSD mean=1/2(CSD pMgx+CSD pNix).

Table 2. Chemical composition of experimental solutions after hydrothermal treatment and Ni/Mg partition coefficient between saponite and solution ($\log D_{\text{Ni-Mg}}$; see text for details)

Series	Samples	Solution chemistry (ppm)				pH _i	pH _f	$\log D_{\text{Ni-Mg}}$
		Si	Mg	Ni	Al			
(pMg150+pNi150)150	(pMg150+pNi150)150–0d	7.764	3.002	0.003	0.157	8.24	8.24	3.38
	(pMg150+pNi150)150–14d	7.189	3.612	0.002	0.173	8.24	8.18	3.64
	(pMg150+pNi150)150–30d	5.666	2.234	0.005	0.232	8.23	8.15	3.03
(pMg220+pNi220)220	(pMg220+pNi220)220–0d	8.060	1.882	0.007	0.269	8.59	8.59	
	(pMg220+pNi220)220–30d	21.614	1.390	0.002	0.198	8.59	7.50	
	(pMg220+pNi220)220–90d	10.260	0.713	0.007	0.094	8.61	9.79	
(pNi220+pMg25)220	(pNi220+pMg25)220–0d	7.491	94.109	0.002	0.139	8.78	8.78	
	(pNi220+pMg25)220–60d	12.260	7.653	0.001	0.124	8.78	8.17	
(pMg220+pNi25)220	(pMg220+pNi25)220–0d	11.699	3.598	0.297	0.069	8.10	8.10	1.46
	(pMg220+pNi25)220–60d	11.611	15.001	0.003	0.090	8.10	7.74	4.08

pH_i and pH_f correspond to the pH of solution at the beginning of hydrothermal treatment and the pH of solution after hydrothermal treatment, respectively.

KBr salt. The mixture was pressed for 5 min at 8 kbar and dried overnight in an oven at 120°C. Spectral manipulations were performed using the OMNIC software package. Before fitting the structural OH, a baseline between 3600 and 3700 cm^{-1} was created to largely exclude the influence of water. The experimental spectra were iteratively fitted using the Gauss–Lorentz cross-product function by varying the width and shape of four structural OH stretching vibrations (Mg_3OH , Mg_2NiOH , Ni_2MgOH , Ni_3OH) until the squared correlation coefficients $r^2 \geq 0.995$, as described in Zhang et al. (2020, 2021) and shown in Fig. 3. Then, the band positions and areas were extracted. The relative area $R_{(\text{IR})}$ is an indicator of cation mixing in the trioctahedral-like sheets. The $R_{(\text{IR})}$ was measured by the ratio of the area of the bands involving Mg and Ni neighbors, i.e. $R_{(\text{IR})} = [(S_{\text{Mg}_2\text{NiOH}} + S_{\text{Ni}_2\text{MgOH}})] / [(S_{\text{Mg}_3\text{OH}} + S_{\text{Mg}_2\text{NiOH}} + S_{\text{Ni}_2\text{MgOH}} + S_{\text{Ni}_3\text{OH}})]$, where S refers the integral area of each band. The Mg and Ni are equimolar in each sample, so for a random distribution of cations in trioctahedral sites around structural-OH, the theoretical ratio of bands $\text{Mg}_3\text{OH}/\text{Mg}_2\text{NiOH}/\text{Ni}_2\text{MgOH}/\text{Ni}_3\text{OH}$ is 0.125/0.375/0.375/0.125, giving $R_{(\text{theory})} = 0.75$. The $R_{(\text{IR})}/R_{(\text{theory})} = 0$ corresponds to the mechanical mixture of Mg-saponite and

Ni-saponite; while $R_{(\text{IR})}/R_{(\text{theory})}$ close to 1 is indicative of a total transformation of Mg- and Ni-saponite into Mg-Ni saponite solid solution. The ratio $R_{(\text{IR})}/R_{(\text{theory})} = \text{precursor dissolution extent (DE)}$ can be used to estimate the level of reaction between the precursors (Zhang et al., 2021) (see Table 3). DE of ~ 0.8 stands for a total dissolution of precursors and recrystallization of Mg-Ni saponite (Zhang et al., 2021). To convert relative areas to occupancies and DE, we assume that the extinction coefficients of the four bands are identical, a common assumption for phyllosilicates (e.g. Petit et al., 2004).

High-angle annular dark-field scanning transmission electron microscopy (HAADF-STEM) observations were performed to investigate the morphology in the *ab* direction of the saponite particles. One milligram of sample was soaked in 10 mL of deionized water with slight stirring for 1 week to obtain a dilute colloidal suspension. Specimens were prepared by dispersing the colloidal suspension in 40 mL of ethanol and ultrasonically treating for 10 min. A drop of the resultant suspension was placed on a porous carbon film supported by a copper grid, and the water and ethanol were then evaporated. STEM images were obtained using a FEI Talos F200S high-

Table 3. Degree of random distribution of octahedral cations ($R_{(IR)}$) and precursor dissolution extent (DE) (see text) for all synthetic Mg-Ni saponites and their corresponding precursors

Series	Samples	$R_{(IR)}$	DE
(pMg150+pNi150)150	(pMg150+pNi150)150-0d	~0.13	~0.17
	(pMg150+pNi150)150-14d	0.25	0.33
	(pMg150+pNi150)150-30d	0.31	0.41
(pMg220+pNi220)220	(pMg220+pNi220)220-0d	~0.00	~0.00
	(pMg220+pNi220)220-30d	~0.00	~0.00
	(pMg220+pNi220)220-90d	~0.00	~0.00
(pNi220+pMg25)220	(pNi220+pMg25)220-0d	~0.00	—
	(pNi220+pMg25)220-60d	~0.00	—
(pMg220+pNi25)220	(pNi25+pMg220)220-0d	~0.00	~0.00
	(pNi25+pMg220)220-60d	0.36	0.48

resolution transmission electron microscope (HRTEM) operated at 200 kV. The energy dispersive X-ray spectra (EDXS) were acquired in HAADF-STEM mode to analyze the chemical composition of the samples.

Results

XRD data

For all series of the synthetic samples, their powder XRD patterns (Fig. 1) display characteristic reflections of tri-octahedral Na-smectite with the (001) reflection at ~ 1.25 nm, the (06,33) band at 0.153 nm and asymmetric (hk) bands (e.g. Brown, 1980). The (001) reflection gradually becomes sharper and narrower with synthesis time increasing, corresponding to an increase of the

stacking layers in saponite particles. For samples (pMg150+pNi150)150-0d and (pMg220+pNi220)220-0d, the measured crystal size dimensions (CSD) are equivalent to the CSD mean of the mechanically mixed Mg- and Ni-saponite precursors that are obtained at the same temperature (Fig. 1a,b; Table 1) (Zhang *et al.*, 2021). For samples (pMg220+pNi25)220-0d and (pNi220+pMg25)220-0d, the measured CSD is closer to the CSD of the well-crystallized precursors, pMg220 and pNi220, respectively (Fig. 1c,d; Table 1). Except for the Series (pMg220+pNi220)220, an increase in crystallinity in the layer plane is observed in all other series with synthesis time increasing (Table 1).

FTIR data

The four structural OH, i.e. Mg_3OH , Mg_2NiOH , $MgNi_2OH$, and Ni_3OH , which correspond to the four possible combinations of octahedral cations around each OH, exhibit stretching vibrations at 3675, 3663, 3648, and 3628 cm^{-1} , respectively (e.g. Petit and Madejová, 2013). Series (pMg150+pNi150)150, 0d-sample, exhibits the dominant νMg_3OH and νNi_3OH bands, consistent with the mechanical mixture of pNi150 and pMg150 precursors (Fig. 2a). With increase in synthesis time, four expected OH-stretching vibrations occur, with a prominent intensity increase of the νMg_2NiOH and $\nu MgNi_2OH$ bands. For Series (pMg220+pNi220)220 (Fig. 2b), only the two νMg_3OH and νNi_3OH bands are observed in all samples whatever the synthesis time.

A shoulder at 3648 cm^{-1} attributed to $\nu MgNi_2OH$ vibration is also observed in both (pMg150+pNi150)150-0d and (pMg220+pNi220)220-0d samples, due to small numbers of neighboring Mg-Ni cations in the octahedral sheet, formed during the 1-day mixing step of precursors at room temperature (Zhang *et al.*, 2020).

The sample (pNi220+pMg25)220-0d (Fig. 2c) displays a broad band due to Mg_3OH and a narrow and sharp νNi_3OH band. Conversely, a broad band due to νNi_3OH and a narrow and sharp νMg_3OH band are observed for the sample (pMg220+pNi25)220-

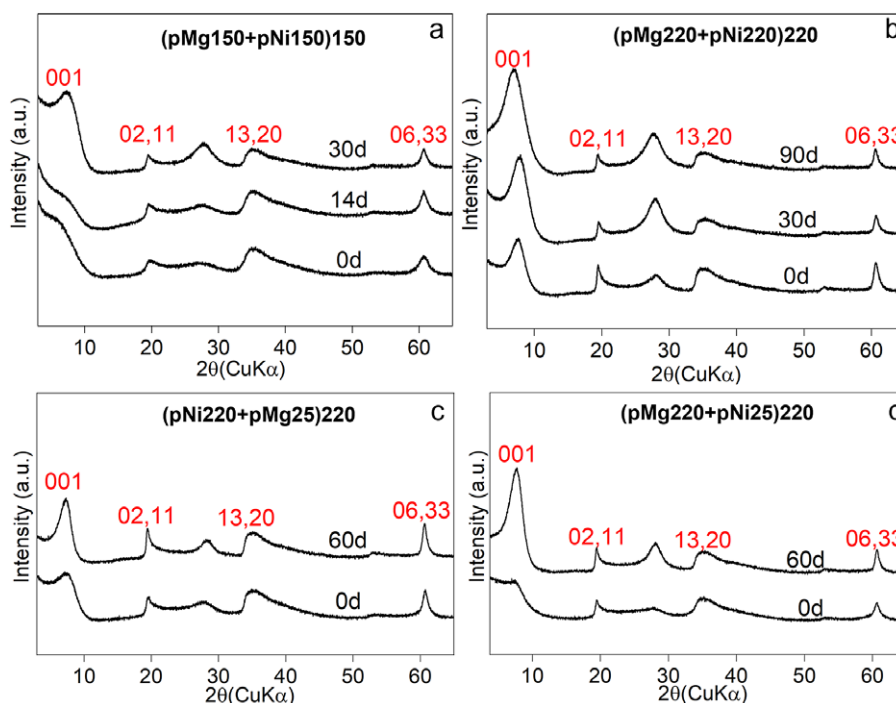


Figure 1. Powder XRD patterns of synthetic saponites. (a) Series (pMg150+pNi150)150; (b) Series (pMg220+pNi220)220; (c) Series (pNi220+pMg25)220; (d) Series (pMg220+pNi25)220.

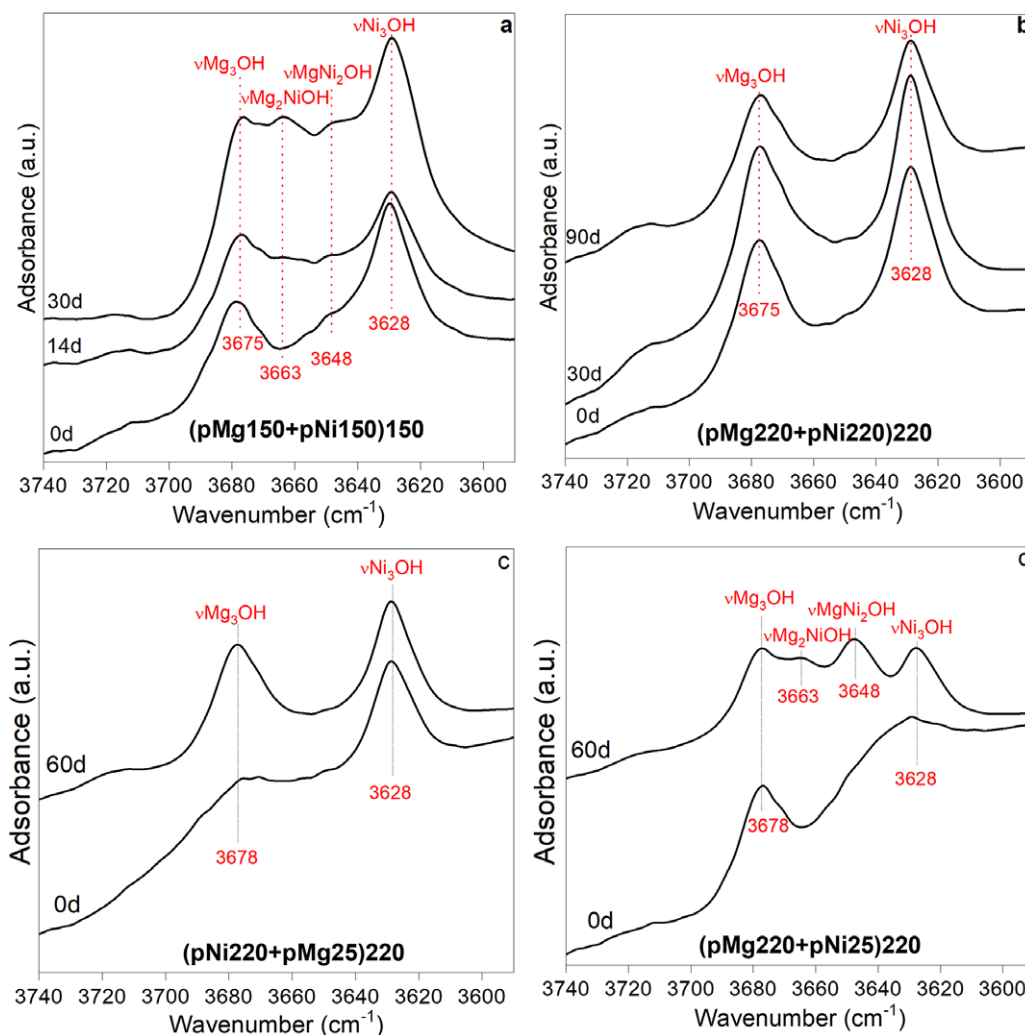


Figure 2. Structural OH-stretching vibration region of the FTIR spectra of synthetic samples. (a) Series (pMg150+pNi150)150; (b) Series (pMg220+pNi220)220; (c) Series (pNi220+pMg25)220; (d) Series (pMg220+pNi25)220.

+pNi25)220-0d (Fig. 2d). The broadening of the ν_{M_3OH} bands of pM25 (M being Mg or Ni) precursors are associated with their faulty structure (Table 1). The observed spectra for the 0d samples accord well with the mechanical mixture of the precursors with different crystallinity (Zhang et al., 2021). For Series (pNi220+pMg25)220, the ν_{Mg_3OH} shoulder becomes narrow and sharp for the 60-day sample, whereas the ν_{Ni_3OH} band does not vary significantly (Fig. 2c). In this sample, the lack of ν_{MgNi_2OH} and ν_{Mg_2NiOH} bands suggests a mixture of pure Ni-saponite and Mg-saponite particles. In sample (pMg220+pNi25)220-60d, the four OH-stretching vibrations are observed (Fig. 2d). The broad shoulders observed in the 3710 cm^{-1} regions are probably attributed to the exchange of Na from smectite by K from KBr used for pellet preparation (Pelletier et al., 1999), and its contribution to the analysis of the relative band areas is considered negligible. All the structural OH regions ($3600\text{--}3700\text{ cm}^{-1}$) were fitted to calculate $R_{(IR)}$ (Fig. 3).

STEM results

Samples of Series (pMg150+pNi150)150 (Fig. 4a,b) are difficult to disperse into recognizable separate particles compared with those of Series (pMg220+pNi220)220 (Fig. 4c,d). Sample (pMg150+pNi150)150-0d consists of aggregates of 5–20 nm

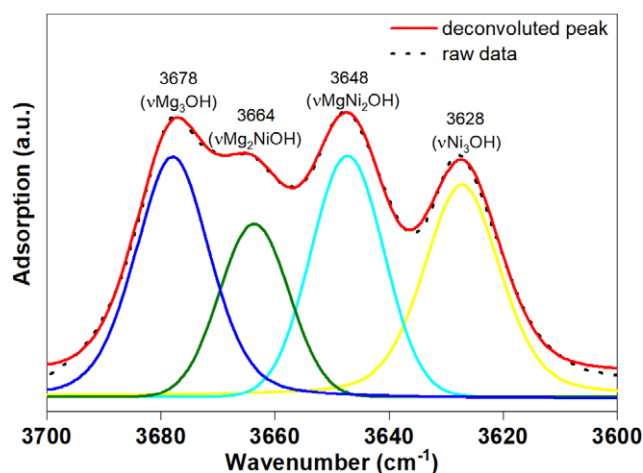


Figure 3. Decomposition of the MIR spectra in the vOH region, sample (pMg220+pNi25)220-60d as an example.

small particles with shapeless morphology (Fig. 4a). After 30 days of synthesis, the particles with a size of $>50\text{ nm}$ are widespread, but many blurry aggregates still exist (Fig. 4b). For Series (pMg220+pNi220)220 (Fig. 4c,d), there is no

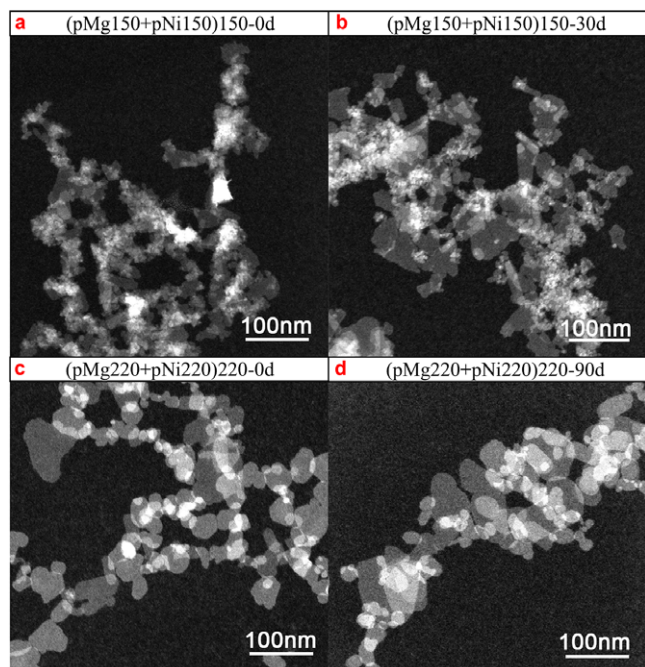


Figure 4. HAADF-STEM images of synthetic saponites in Series 150-150 and 220-220. Samples: (a) (pMg150+pNi150)150-0d; (b) (pMg150+pNi150)150-30d; (c) (pMg220+pNi220)220-0d; (d) (pMg220+pNi220)220-90d.

noticeable change in particle size and morphology between 0- and 90-day samples, and a particle size of 10–120 nm is clearly observed.

The precursors pMg25 and pNi25 did not disperse well, and shapeless particles (<50 nm) are observed (Fig. 5a,d). Most particles in pNi220 (Fig. 5b) are rounded and homogeneous

with a size of 10–50 nm; few are larger than 50 nm and exhibit sub-hexagonal facies. Although pMg220 and pNi220 have similar particle size (Fig. 5b,e), pMg220 has more elongated layers compared with pNi220. In the sample (pNi220+pMg25)220-60d, the majority of particles surpass 30 nm, with several extending up to 120 nm (Fig. 5c). Conversely, in the (pMg220+pNi25)220-60d sample, particles range from 10 to 150 nm (Fig. 5f), with a notable proportion exceeding 50 nm. Saponite layers with dark inner and brightness rims are widespread in sample (pMg220+pNi25)220-60d (Fig. 6a,d). The EDX results indicate that the dark interior consists of Mg-rich saponite units, whereas the brighter rim consists Mg- and Ni-rich saponite units (Fig. 6b,c,e,f).

Solution chemistry

The evolution of the initial pH (pH_i , the pH of solution at the beginning of hydrothermal treatment), final pH (pH_f , the pH of solution after hydrothermal treatment), and aqueous concentrations of Si, Mg, Ni, and Al are presented in Table 2. For 0-day samples, pH_i is similar to pH_f . For other syntheses, the pH_f values are smaller than pH_i values, except for sample (pMg220+pNi220)220-90d, for which the high pH_f value probably resulted from water escaping during the longest period of hydrothermal treatment. Compared with pH_i , lower pH_f is related to OH group consumption during the dissolution of precursors and the recrystallization of hydroxylated minerals (Decarreau, 1985). The higher Mg concentration for sample (pNi220+pMg25)220-0d and higher Ni concentration for (pMg220+pNi25)220-0d sample are attributed to the fast dissolution of pMg25 and pNi25 during the first day of stirring at room temperature, respectively. Considering the volume of fluid and the element concentration in solution, the chemical composition of the synthesized samples are probably very close

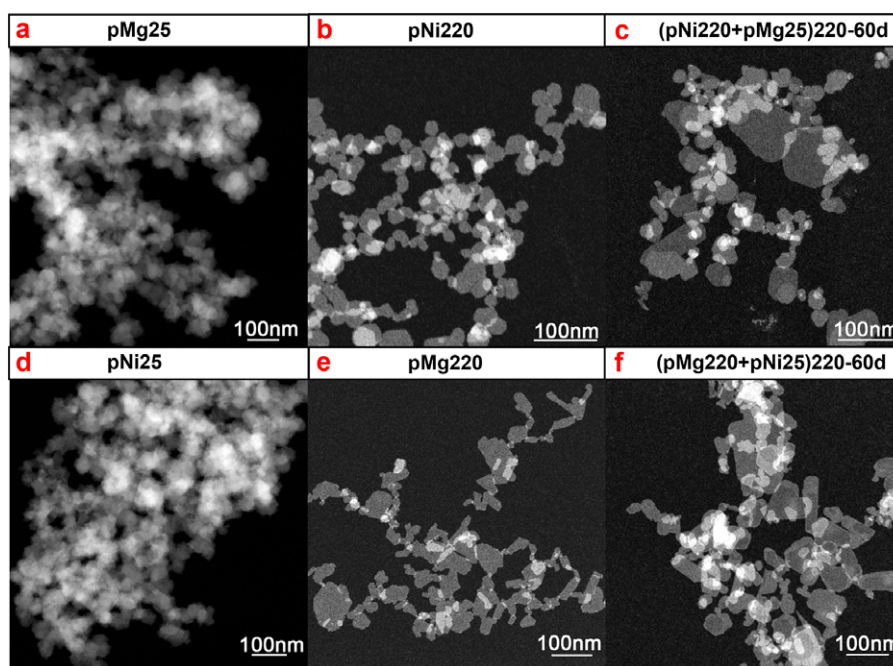


Figure 5. HAADF-STEM images of synthetic saponites and their corresponding precursors: pMg25 (a) and pNi220 (b) are the precursors of sample (pNi220+pMg25)220-60d (c); pNi25 (d) and pMg220 (e) are the precursors of sample (pMg220+pNi25)220-60d (f).

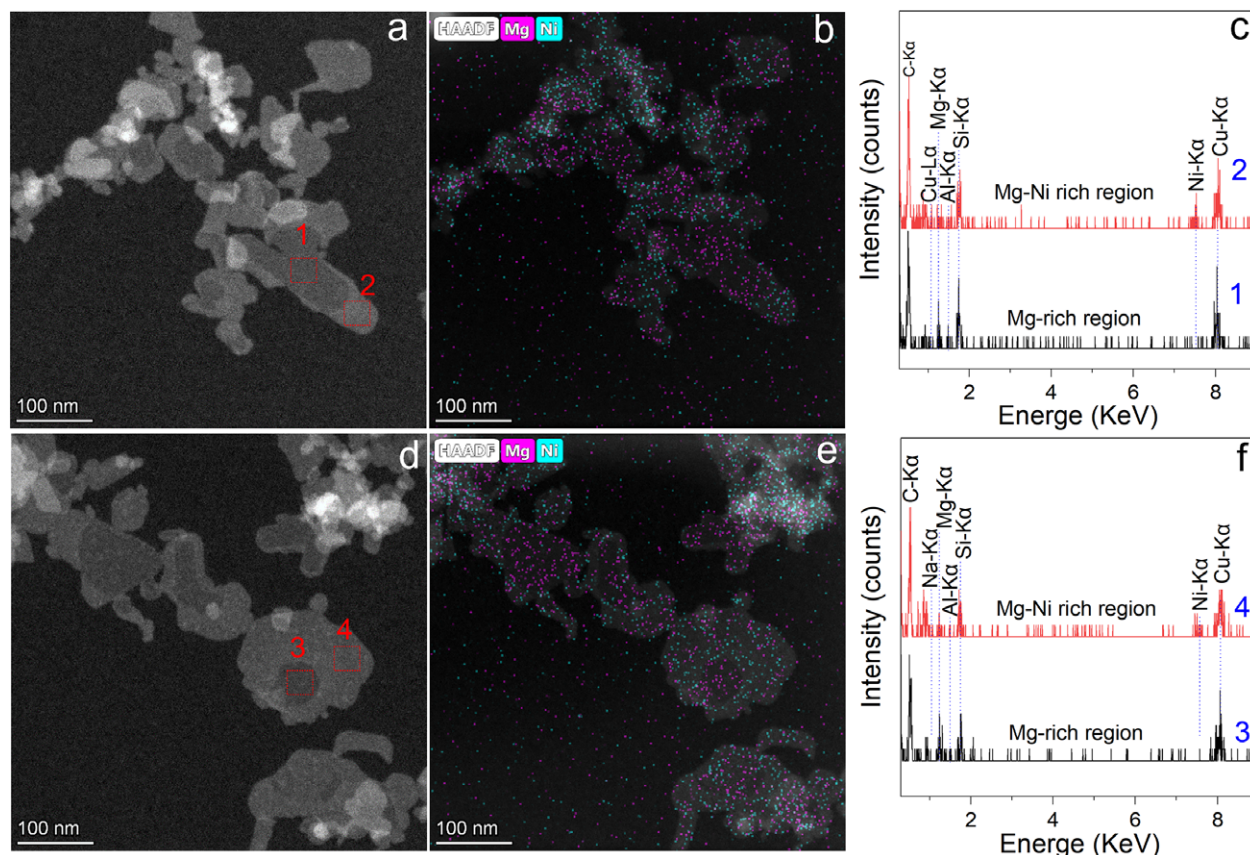


Figure 6. HAADF-STEM images and the corresponding EDXS mapping of synthetic saponite particles of sample (pMg220+pNi25)220-60d. (a,d) HAADF-STEM images of dispersed saponites; (b,e) element mapping overlap of Mg and Ni; (c,f) original EDXS spectra of the regions marked in panels a and d.

to the theoretical composition expected for the saponite ($\text{Na}_{0.3}[\text{Si}_{3.7}\text{Al}_{0.3}][\text{Ni}_{1.5}\text{Mg}_{1.5}\text{O}_{10}(\text{OH})_2$).

Discussion

Crystal growth of saponites

The end of synthesis solutions contain small amounts of Si, Al, Mg, and Ni (Table 2), suggesting that the synthesized solid phases contain almost all the structural elements. FTIR spectra of starting materials (0-day samples) with mainly $\nu\text{Ni}_3\text{OH}$ and $\nu\text{Mg}_3\text{OH}$ bands are consistent with a mechanical mixing of Ni-saponite and Mg-saponite precursors. After the hydrothermal synthesis, Mg-Ni saponite solid solutions were obtained in the series (pMg150+pNi150)150 and (pMg220+pNi25)220, while in the series (pMg220+pNi220)220 and (pNi220+pMg25)220 no saponite solid solutions are observed. The appearance of the $\nu\text{Mg}_2\text{NiOH}$ and $\nu\text{MgNi}_2\text{OH}$ bands in some samples indicate the formation of Ni-Mg saponite particles, produced by the dissolution of the precursor.

Series (pMg150+pNi150)150 and (pMg220+pNi220)220

For the Series (pMg150+pNi150)150, the coarse particles (Fig. 4a, b) and the increase of CSD values (Table 1) give evidence of the crystal growth of Mg-Ni saponite. After 30 days of synthesis, the precursor dissolution extent (DE) is 0.41 (Table 3), indicating that saponite growth dominates by the dissolution of endmember saponite precursors and crystallization of Mg-Ni saponites. The

less than 0.75 DE value indicates that the dissolution of endmember saponite precursor is partial. For the Series (pMg220+pNi220)220, no reaction between the precursors could be observed ($\text{DE} \approx 0$, Table 3). After 90 days of synthesis, the particle size and crystallinity remain similar. The main difference between both series is the particle size (Fig. 4a,c) and crystallinity (Table 1) of precursors. Comparing with the precursors of the (pMg150+pNi150)150 series, those of the (pMg220+pNi220)220 series have a relatively large particle size and CSD, which limit the dissolution of pMg220 and pNi220 precursors and thus prevent the formation of Mg-Ni saponite solid solution. However, small particles of pMg150 and pNi150 precursors drive the dissolution–recrystallisation of precursors, as small particles have a greater surface energy than larger ones (Trolard and Tardy, 1987; McHale et al., 1997; Tang et al., 2004; Navrotsky et al., 2008). This rapid process led to the formation of saponite solid solution.

Series (pNi220+pMg25)220 and (pMg220+pNi25)220

For both series, the syntheses were performed at 220°C for 60 days. The hydrothermal synthesis induces an increase in both particle size (Fig. 5) and crystallinity of the saponite (Table 1). However, a different evolution of crystal chemistry is observed between the two series. For sample (pNi220+pMg25)220-60d, no $\nu\text{Mg}_2\text{NiOH}$ and $\nu\text{MgNi}_2\text{OH}$ are observed (Fig. 2c), indicating no reaction between pNi220 and pMg25 ($\text{DE} \sim 0.00$) (Table 3). The narrowing of the $\nu\text{Mg}_3\text{OH}$ band from 0 days to 60 days (Fig. 2c) implies that pMg25 particles evolves towards a

better crystalline structure as observed by XRD (Fig. 1 and Table 1). The Mg-saponite precursor (pMg25), which is amorphous-like saponite germ, transforms into Mg-saponite independently to initial pNi220 saponite. The unchanged $\nu\text{Ni}_3\text{OH}$ band from 0 days to 60 days (Fig. 2c) indicates that pNi220 particles keep a quasi-steady state. For the (pMg220+pNi25)220-60d sample, the occurrence of $\nu\text{Mg}_2\text{NiOH}$ and $\nu\text{MgNi}_2\text{OH}$ bands (Fig. 2d) and the DE value of 0.48 (Table 3) clearly indicate a partial dissolution of precursors and the formation of large Mg-Ni saponite particles.

In the (pNi220+pMg25)220 and (pMg220+pNi25)220 series, the precursors obtained at 25°C consist of amorphous-like saponite germs (Table 1) (Zhang *et al.*, 2021). These substances readily dissolve, even at room temperature, resulting in elevated Ni or Mg concentrations in the solution for the 0-day samples compared with other series (Table 2). Therefore, the chemical reactions during syntheses can be expressed as $\text{pMg220} + \text{Ni}^{2+}$ and $\text{pNi220} + \text{Mg}^{2+}$. When Mg and Ni cations compete to enter a saponite solid solution, Ni is strongly stabilized in the solid phase, so that the partition coefficient $D_{(\text{Ni-Mg})} = (\text{Ni/Mg})_{\text{solid}} / (\text{Ni/Mg})_{\text{liquid}}$ reaches a relatively high value ($\log D = 2.3$ at 25 and 75°C) (Decarreau, 1985). Partition coefficients in the same range were calculated based on the chemistry of the solution after synthesis, by assuming that a $(\text{Ni/Mg})_{\text{solid}}$ is 1 when a Mg-Ni saponite solid solution was obtained (Table 2). The higher log D values than previously published results from Decarreau (1985) are mainly due to the higher synthesis temperatures (i.e. 150 or 220°C compared with 25 and 75°C) and indicate a stronger Ni stabilization in saponite with the increasing temperature. Thus, for the (pMg220+pNi25)220 series, Ni^{2+} enters the Mg-saponite easily to reach the stable Ni-Mg solid solution. Such reactions were supported by the elemental distribution within the single layer of sample (pMg220+pNi25)220-60d identified with HAADF-STEM and EDXS (Fig. 6), which is similar to the mineral replacement reaction described by Putnis (2002). On the contrary, for the (pNi220+pMg25)220 series, aqueous Mg^{2+} is hard to incorporate into the Ni-saponite so that pMg25 and pNi220 precursors evolve separately.

Considering all sets of experiments, only a few syntheses successfully achieve a stable Mg-Ni saponite solid solution. In the cases of the (pMg150+pNi150)150 and (pMg220+pNi220)220 series, the chemical compositions of the solutions remain consistent and unaltered throughout the synthesis process (Table 2). Thus, the key factor is the dissolution rate of precursors, which is linked to their particle size and crystallinity. At 220°C, the dissolution rate of both pNi220 and pMg220 is notably slow, thereby preventing the formation of Ni-Mg saponite solid solutions. However, the Mg-Ni saponite solid solution was obtained when the same precursors (pNi220 and pMg220) were treated at 300, 400 and 500°C (Zhang *et al.*, 2021), indicating that synthesis temperatures higher than those used for the precursor synthesis facilitate the dissolution of precursors. On the other hand, pNi150 and pMg150 precursors have a smaller particle sizes and a lower crystallinity than those formed at 220°C (Table 1), which promote their dissolution and favor the solid solution formation even at a 150°C synthesis temperature. As mentioned above, the lack of solid solution for the (pNi220+pMg25)220 series is mainly due to the strong stabilization of Ni with regard to Mg in saponite crystals.

Two main points can be highlighted. First, having a zero temperature gap ($\Delta T = 0$) between sample synthesis and precursor preparation is not sufficient to prevent the reaction

between precursors during saponite hydrothermal synthesis, as observed in the (pMg150+pNi150)150 series. Second, the stable thermodynamic phase, here Ni-Mg saponite solid solution, is not necessarily formed, as observed for both (pMg220+pNi220)220 and (pNi220+pMg25)220 series, despite the relatively high temperature (220°C) and synthesis times as long as 2 or 3 months. Klopogge *et al.* (1999) noted that the synthesis duration is generally not sufficient to ascertain that synthetic products are the thermodynamically stable phases.

Kinetic of precursor dissolution

By combining present data and previous results obtained with the same chemical system $\text{Na}_{0.3}[\text{Si}_{3.7}\text{Al}_{0.3}][\text{Ni}_{1.5}\text{Mg}_{1.5}]\text{O}_{10}(\text{OH})_2$, but with other synthesis conditions (Zhang *et al.* 2020; Zhang *et al.*, 2021), it is possible to predict the kinetic dissolution and crystal growth of saponite during syntheses.

The mixture of pNi150 and pMg150 precursors was hydrothermally treated for 30 days at 150 and 220°C (Zhang *et al.*, 2020). Both the (pMg150+pNi150)150 and (pMg150+pNi150)220 series displayed a similar trend depicted by a logarithm function (Fig. 7a). After a rapid increase up to ~5 days of synthesis, DE increases very slowly when increasing the synthesis time. Raising the synthesis temperature from 150 to 220°C leads to a significant increase in DE values (DE=0.41 and 0.73, respectively). For the synthesis from the mixture of pNi25 and pMg220 precursor, the DE value remains low (0.48) even after 60 days of synthesis at 220°C (Fig. 7a). All the results seen in Fig. 7a suggest that extending the synthesis time would not induce a significant evolution of saponite once the DE value reached a plateau.

Zhang *et al.* (2021) synthesized a series of saponites at 220°C for 14 days with precursors gradually changing from pNi25+pMg25 to pNi220+pMg220 (temperature of precursors=25, 50, 150, 180, 200, 220°C) (empty triangles in Fig. 7a,b). These data clearly illustrate the influence of ΔT on DE of saponite precursors. The DE value increases with increase in ΔT values (Fig. 7b). The highest values of ΔT correspond to the syntheses with the precursors prepared at low temperatures (25 and 50°C) (Zhang *et al.*, 2021).

Another series was obtained by hydrothermally treating the same starting material pNi220+pMg220 for 7 days at various temperatures (220, 300, 400, and 500°C) (Zhang *et al.*, 2021). The DE value increases as the synthesis temperature rises (Fig. 7c) but the slope of the curve decreases with increasing T . During a high temperature system, an increase of T would not induce a significant progress in crystal growth because (Mg)-saponite is stable up to ~600°C (Iiyama and Roy, 1963; Zhang *et al.*, 2010; Meyer *et al.*, 2020).

The above results show that, for the studied series, an increase in synthesis time, synthesis temperature, or ΔT , the other parameter being constant, would not be enough to significantly increase the crystal growth of saponite. The prominent feature is the quasi-steady-state reached after about 2 weeks of synthesis.

The DE value is efficient at estimating the crystal growth of saponite within a series but cannot be applied for comparison between series. For example, after synthesis of mixture pNi50+pMg50 at 220°C (Fig. 7a), DE=0.8 and the diameter of saponite particles is 40–150 nm while for the pNi220+pMg220 precursor treated at 500°C, DE=0.72 and particles reach 400 nm in diameter (Zhang *et al.*, 2021; Fig. 7c).

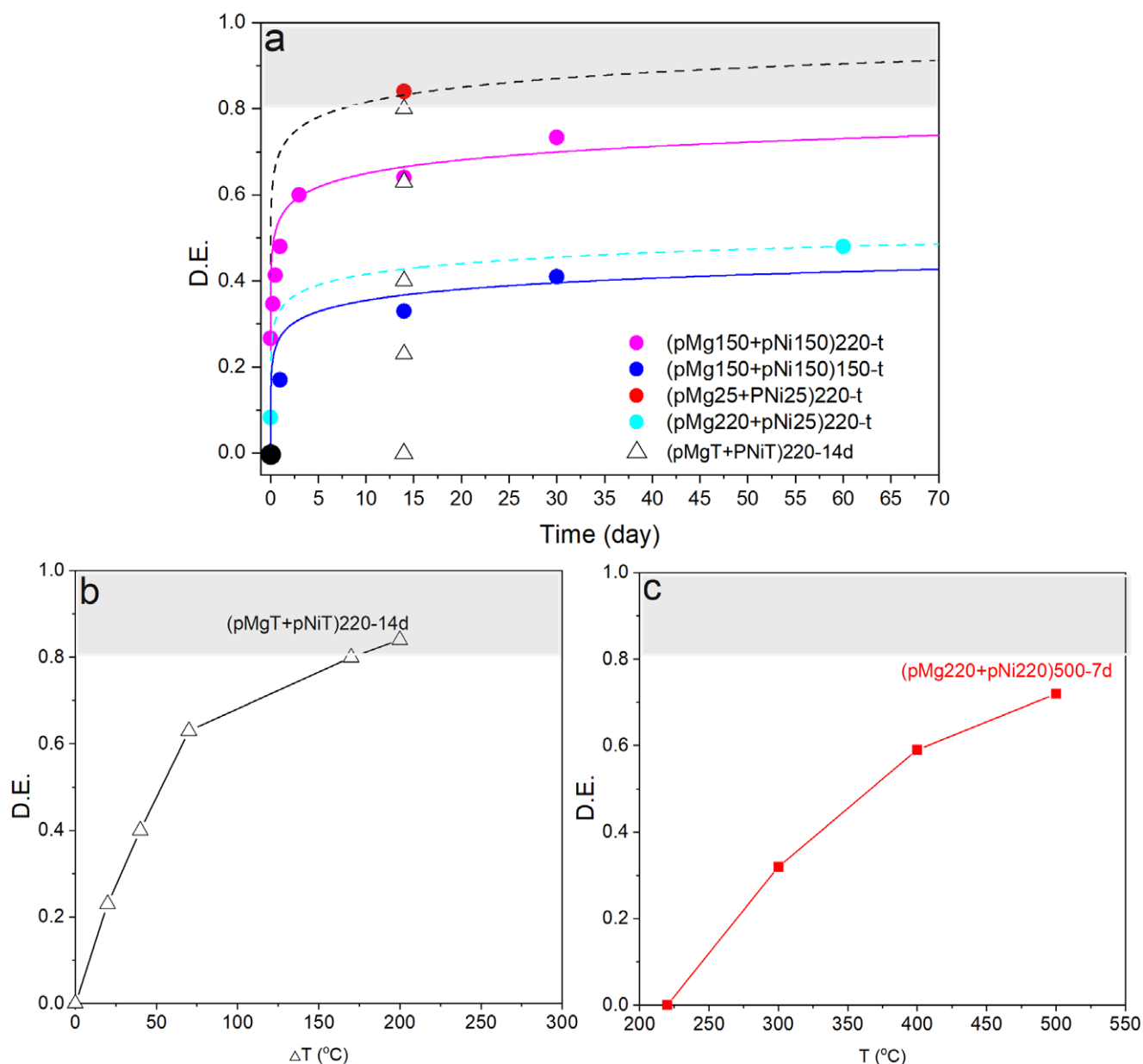


Figure 7. Relationships between precursor dissolution extent (DE) and synthesis factors. The grey zone corresponds to a total dissolution of precursors. (a) DE vs synthesis time. Data for (pMg220+pNi25)220-t and (pMg150+pNi150)150-t series are taken from Table 3; data for (pMg25+pNi25)220-t and (pMg150+pNi150)220-t series are from Zhang et al. (2020); empty triangles correspond to the (pMgT+pNiT)220-14d series (Zhang et al., 2021). Continuous line: logarithmic curve traced to indicate the series evolution trend from several experimental data. Dashed line: logarithmic curve traced to indicate the hypothetical series evolution trend. The black filled circle is shared by all the series. (b) DE vs ΔT (the temperature gap between the precursors prepared and the resultant Mg-Ni saponite obtained) for the (pMgT+pNiT)220-14 series (data from Zhang et al., 2021). (c) DE vs T (the temperature of hydrothermal treatment for the (pMg220+pNi220)T-7d series) (data from Zhang et al., 2021).

Author contribution. Sabine Petit and Hongping He designed this research; Chaoqun Zhang, Fabien Baron, Brian Gregoire, and Yuhuan Yuan prepared the samples and performed all the experiments; Chaoqun Zhang, Alain Decarreau, Sabine Petit, and Hongping He analyzed the data and wrote the manuscript. All authors participated in the discussion.

Acknowledgements. We thank the anonymous reviewers for their constructive comments, which greatly improve this paper.

Financial support. We appreciate the financial support of the National Natural Science Foundation of China (grant nos 42202265, 42202261, 42272038), Student Research Grant of the Clay Minerals Society, and China Scholarship Council, the French government programme 'Investissements d'Avenir' (EUR INTREE, reference ANR-18-EURE-0010), and the European Union (ERDF) and 'Région Nouvelle Aquitaine'.

Competing interests. The authors declare that they have no known competing financial interests or personal relationships that could have appeared to influence the work reported in this paper.

Data availability statement. All data needed to evaluate the conclusions in the paper are present in the main manuscript. The original data can be found in 10.6084/m9.figshare.27147597

References

- Besselink, R., Stawski, T.M., Freeman, H.M., Hövelmann, J., Tobler, D.J. & Benning, L.G. (2020). Mechanism of saponite crystallization from a rapidly formed amorphous intermediate. *Crystal Growth & Design*, 20, 3365–3373.

- Blukis, R., Schindler, M., Couasnon, T., & Benning, L.G. (2022). Mechanism and control of saponite synthesis from a self-assembling nanocrystalline precursor. *Langmuir*, 38, 7678–7688.
- Brigatti, M.F., Galán, E., & Theng, B.K.G. (2013). Chapter 2 – Structure and mineralogy of clay minerals, pp. 21–81. In F. Bergaya and G. Lagaly (eds), *Developments in Clay Science*. Elsevier.
- Brown, G., & Brindley, G.W. (1980). *Crystal Structures of Clay Minerals and their X-ray Identification*. Monograph no. 5, Mineralogical Society, London.
- Butt, C.R.M., & Cluzel, D. (2013). Nickel laterite ore deposits: weathered serpentinites. *Elements*, 9, 123–128.
- Carter, J., Poulet, F., Murchie, S., & Bibring, J.P. (2013). Automated processing of planetary hyperspectral datasets for the extraction of weak mineral signatures and applications to crism observations of hydrated silicates on mars. *Planetary and Space Science*, 76, 53–67.
- Couty R., Decarreau A., & Perruchot A. (1981). Etude par spectroscopie infrarouge de l'évolution de précipités silico-magnésiens conduisant à la formation de stévensites. *Comptes Rendus de l'Académie des Sciences*, 292, 1269–1272.
- Decarreau, A. (1980). Cristallogénèse expérimentale des smectites magnésiennes: hectorite, stévensite. *Bulletin de minéralogie*, 103, 579–590.
- Decarreau, A. (1985). Partitioning of divalent transition-elements between octahedral sheets of trioctahedral smectites and water. *Geochimica et Cosmochimica Acta*, 49, 1537–1544.
- Ehlmann, B.L., Berger, G., Mangold, N., Michalski, J.R., Catling, D.C., Ruff, S.W., Chassefière, E., Niles, P.B., Chevrier, V., & Poulet, F. (2013). Geochemical consequences of widespread clay mineral formation in mars' ancient crust. *Space Science Reviews*, 174, 329–364.
- Ehlmann, B.L., & Edwards, C.S. (2014). Mineralogy of the martian surface, pp. 291–315. In R. Jeanloz (Ed), *Annual Review of Earth and Planetary Sciences*, vol. 42.
- Ferrage, E. (2016). Investigation of the interlayer organization of water and ions in smectite from the combined use of diffraction experiments and molecular simulations. A review of methodology, applications, and perspectives. *Clays and Clay Minerals*, 64, 348–373.
- Fritsch, E., Juillot, F., Dublet, G., Fonteneau, L., Fandeur, D., Martin, E., Caner, L., Auzende, A.L., Grauby, O., & Beaufort, D. (2016). An alternative model for the formation of hydrous Mg/Ni layer silicates ('deweylite'/i'garnierite') in faulted peridotites of New Caledonia: I. Texture and mineralogy of a paragenetic succession of silicate infillings. *European Journal of Mineralogy*, 28, 295–311.
- Gaudin, A., Petit, S., Rose, J., Martin, F., Decarreau, A., Noack, Y., & Borschneck, D. (2004). The accurate crystal chemistry of ferric smectites from the lateritic nickel ore of Murrin Murrin (Western Australia). II. Spectroscopic (IR and EXAFS) approaches. *Clay Minerals*, 39, 453–467.
- He, H.P., Li, T., Tao, Q., Chen, T.H., Zhang, D., Zhu, J.X., Yuan, P., & Zhu, R.L. (2014). Aluminum ion occupancy in the structure of synthetic saponites: effect on crystallinity. *American Mineralogist*, 99, 109–116.
- Hover, V.C., Walter, L.M., Peacor, D.R., & Martini, A.M. (1999). Mg-smectite authigenesis in a marine evaporative environment, Salina Ometepec, Baja California. *Clays and Clay Minerals*, 47, 252–268.
- Iiyama, J.T., & Roy, R. (1963). Unusually stable saponite in the system Na₂O-MgO-Al₂O₃-SiO₂. *Clay Minerals Bulletin*, 5, 161–171.
- Kloprogge, J.T., Komarneni, S., & Amonette, J.E. (1999). Synthesis of smectite clay minerals: a critical review. *Clays and Clay Minerals*, 47, 529–554.
- Mano, E.S., Caner, L., Petit, S., Chaves, A.P., & Mexias, A.S. (2019). Ni-smectitic ore behaviour during the caron process. *Hydrometallurgy*, 186, 200–209.
- McHale, J.M., Auroux, A., Perrotta, A.J., & Navrotsky, A. (1997). Surface energies and thermodynamic phase stability in nanocrystalline aluminas. *Science*, 277, 788–791.
- Meyer, S., Bennici, S., Vaulot, C., Rigolet, S., & Dzene, L. (2020). Influence of the precursor and the temperature of synthesis on the structure of saponite. *Clays and Clay Minerals*, 68, 544–552.
- Michalski, J.R., Cuadros, J., Bishop, J.L., Dyar, M.D., Dekov, V., & Fiore, S. (2015). Constraints on the crystal-chemistry of fe/mg-rich smectitic clays on mars and links to global alteration trends. *Earth and Planetary Science Letters*, 427, 215–225.
- Navrotsky, A., Mazeina, L., & Majzlan, J. (2008). Size-driven structural and thermodynamic complexity in iron oxides. *Science*, 319, 1635–1638.
- Pelletier, M., Michot, L.J., Barres, O., Humbert, B., Petit, S., & Robert, J.L. (1999). Influence of KBr conditioning on the infrared hydroxyl-stretching region of saponites. *Clay Minerals*, 34, 439–445.
- Petit, S., Baron, F., & Decarreau, A. (2017). Synthesis of nontronite and other Fe-rich smectites: a critical review. *Clay Minerals*, 52, 469–483.
- Petit, S., & Madejová, J. (2013). Chapter 2.7 – Fourier transform infrared spectroscopy, pp. 213–231. In F. Bergaya and G. Lagaly (eds), *Developments in Clay Science*. Elsevier.
- Petit, S., Martin, F., Wiewiora, A., De Parseval, P., & Decarreau, A. (2004). Crystal-chemistry of talc: a near infrared (NIR) spectroscopy study. *American Mineralogist*, 89, 319–326.
- Putnis, A. (2002). Mineral replacement reactions: from macroscopic observations to microscopic mechanisms. *Mineralogical Magazine*, 66, 689–708.
- Schoonheydt, R.A. (2002). Smectite-type clay minerals as nanomaterials. *Clays and Clay Minerals*, 50, 411–420.
- Tang, R.K., Wang, L.J., & Nancollas, G.H. (2004). Size-effects in the dissolution of hydroxyapatite: an understanding of biological demineralization. *Journal of Materials Chemistry*, 14, 2341–2346.
- Trolard, F., & Tardy, Y. (1987). The stabilities of gibbsite, boehmite, aluminous goethites and aluminous hematites in bauxites, ferricretes and laterites as a function of water activity, temperature and particle-size. *Geochimica et Cosmochimica Acta*, 51, 945–957.
- Warren, C.J., Dudas, M.J., & Abboud, S.A. (1992). Effects of acidification on the chemical-composition and layer charge of smectite from calcareous till. *Clays and Clay Minerals*, 40, 731–739.
- Yamada, H., Yoshioka, K., Tamura, K., Fujii, K., & Nakazawa, H. (1999). Compositional gap in dioctahedral-trioctahedral smectite system: Beidellite-saponite pseudo-binary join. *Clays and Clay Minerals*, 47, 803–810.
- Zhang, C., He, H., Qin, X., Decarreau, A., Baron, F., Tao, Q., Zhu, J., Xi, Y., & Petit, S. (2022) The growth process of saponite: a study based on particle size distributions and morphological evolution. *Applied Clay Science*, 221, 106463.
- Zhang, C.Q., He, H.P., Petit, S., Baron, F., Tao, Q., Gregoire, B., Zhu, J.X., Yang, Y.P., Ji, S.C., & Li, S.Y. (2021). The evolution of saponite: an experimental study based on crystal chemistry and crystal growth. *American Mineralogist*, 106, 909–921.
- Zhang, C.Q., Petit, S., He, H.P., Villieras, F., Razafitianamaharavo, A., Baron, F., Tao, Q., & Zhu, J.X. (2020) Crystal growth of smectite: a study based on the change in crystal chemistry and morphology of saponites with synthesis time. *ACS Earth and Space Chemistry*, 4, 14–23.
- Zhang, D., Zhou, C.H., Lin, C.X., Tong, D.S., & Yu, W.H. (2010). Synthesis of clay minerals. *Applied Clay Science*, 50, 1–11.